Biochimica et Biophysica Acta 1837 (2014) 1932–1943

Contents lists available at ScienceDirect

Biochimica et Biophysica Acta

journal homepage: www.elsevier.com/locate/bbabio

Key roles of the *Escherichia coli* AhpC C-terminus in assembly and catalysis of alkylhydroperoxide reductase, an enzyme essential for the alleviation of oxidative stress

Phat Vinh Dip [a,b,c,1], Neelagandan Kamariah [d,1], Wilson Nartey [a,1], Claudia Beushausen [a], Victor A. Kostyuchenko [b,c], Thiam-Seng Ng [b,c], Shee-Mei Lok [b,c], Wuan Geok Saw [a], Frank Eisenhaber [d,e,f], Birgit Eisenhaber [d], Gerhard Grüber [a,d,*]

[a] Nanyang Technological University, School of Biological Sciences, 60 Nanyang Drive, Singapore 637551
[b] Program in Emerging Infectious Diseases, Duke-NUS Graduate Medical School, KTP Building, 8 College Road, Singapore 169857
[c] Center for Bioimaging Sciences, Dept. of Biological Sciences, National University of Singapore, Singapore 119077
[d] Bioinformatics Institute, Agency for Science, Technology and Research (A*STAR), 30 Biopolis Street, #07-01 Matrix, Singapore 138671
[e] School of Computer Engineering, Nanyang Technological University, 50 Nanyang Drive, Singapore 637553
[f] Department of Biological Sciences, National University of Singapore, 8 Medical Drive, Singapore 117597

ARTICLE INFO

Article history:
Received 12 June 2014
Received in revised form 19 August 2014
Accepted 25 August 2014
Available online 2 September 2014

Keywords:
Reactive oxygen species
Oxidative stress
Alkylhydroperoxide reductase
Redox homeostasis
Structural biology
Electron microscopy

ABSTRACT

2-Cys peroxiredoxins (Prxs) are a large family of peroxidases, responsible for antioxidant function and regulation in cell signaling, apoptosis and differentiation. The *Escherichia coli* alkylhydroperoxide reductase (AhpR) is a prototype of the Prxs-family, and is composed of an NADH-dependent AhpF reductase (57 kDa) and AhpC (21 kDa), catalyzing the reduction of H_2O_2. We show that the *E. coli* AhpC (*Ec*AhpC, 187 residues) forms a decameric ring structure under reduced and close to physiological conditions, composed of five catalytic dimers. Single particle analysis of cryo-electron micrographs of C-terminal truncated (*Ec*AhpC$_{1\text{-}172}$ and *Ec*AhpC$_{1\text{-}182}$) and mutated forms of *Ec*AhpC reveals the loss of decamer formation, indicating the importance of the very C-terminus of AhpC in dimer to decamer transition. The crystallographic structures of the truncated *Ec*AhpC$_{1\text{-}172}$ and *Ec*AhpC$_{1\text{-}182}$ demonstrate for the first time that, in contrast to the reduced form, the very C-terminus of the oxidized *Ec*AhpC is oriented away from the AhpC dimer interface and away from the catalytic redox-center, reflecting structural rearrangements during redox-modulation and -oligomerization. Furthermore, using an ensemble of different truncated and mutated *Ec*AhpC protein constructs the importance of the very C-terminus in AhpC activity and in AhpC–AhpF assembly has been demonstrated.

1. Introduction

Peroxiredoxins (Prxs) are described as the family of peroxidases that is broadly important in both antioxidant protection and cellular signaling pathways [1,2]. Prxs are responsible for the reduction of about 90% of mitochondrial H_2O_2 [3] and almost 100% of cytoplasmic H_2O_2 [2]. These numbers make clear that Prxs are the dominant player in the protection of cells from oxidative stress and explain why they are among the ten most abundant proteins like in *Escherichia coli* [4]. Many bacteria use the alkyl hydroperoxide reductase (AhpR) complex as an essential peroxide-inducible response to oxidative stress [5]. AhpR consists of two enzymes AhpC and AhpF, which together catalyze the NADH-dependent reduction of H_2O_2 to its corresponding alcohols and water [6,7]. AhpF consists of three domains; an N-terminal domain (NTD), a FAD-binding- and an NADH-binding domain, and it acts as a dedicated AhpC reductase (Fig. 1). A compact and an extended AhpF crystal structure from *Salmonella typhimurium* [8] and *E. coli* [9], respectively, has been recently described. AhpC is the peroxidase of the AhpR complex, belonging to the so-called typical 2-Cys peroxiredoxins with two conserved redox-active cysteines. One is called the peroxidatic cysteine (C_P), located at the N-terminus, which attacks the peroxide substrate (ROOH) and becomes oxidized to a sulfenic acid (Fig. 1). The second and C-terminal cysteine of AhpC is the resolving cysteine (C_R). It attacks the cysteine-sulfenic acid to release water and to form a disulfide bond. This disulfide bond is then reduced by AhpF, completing the catalytic cycle (Fig. 1).

AhpCs form a catalytic homodimer, in which the C_P from one monomer and the $C_{R'}$ from the other generate two intersubunit redox-active disulfides. Comparison of the oxidized *S. typhimurium* [10] and *E. coli* AhpC [9] structures on one hand and the reduced *S. typhimurium* AhpC(C47S) mutant structure [11] on the other shows major

* Corresponding author at: Nanyang Technological University, School of Biological Sciences, 60 Nanyang Drive, Singapore 637551. Tel.: +65 6316 2989; fax: +65 6791 3856.
E-mail address: ggrueber@ntu.edu.sg (G. Grüber).
[1] Authors contributed equally to this work.

http://dx.doi.org/10.1016/j.bbabio.2014.08.007
0005-2728/

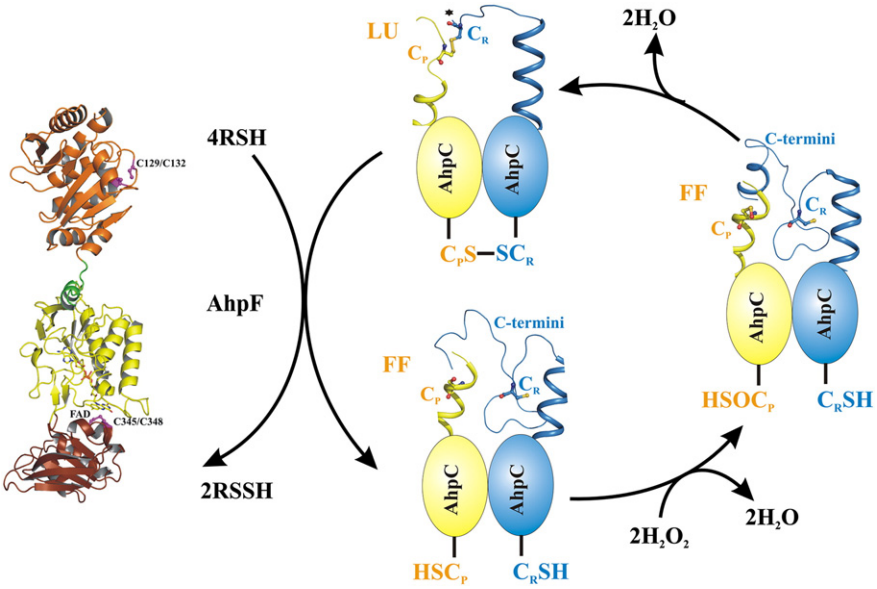

Fig. 1. The proposed catalytic cycle of the AhpC–AhpF complex. The catalytic dimer assembly of AhpC with its different forms of peroxidatic cysteine (C_P) and resolving cysteine (C_R) is shown as they undergo modifications during catalysis. Their corresponding conformations are also represented by ribbon diagrams. FF means that the reduced and sulfenic acid forms of C_P adopted a fully folded conformation. The disulfide bond form adopted a locally unfolded (LU) conformation with the disordered C-termini denoted by asterisks. The NADH-dependent flavoprotein AhpF, here presented in the extended form of the recently determined crystal structure of *E. coli* AhpF ([9]; PDB ID: 4O5Q), regenerates AhpC for further catalysis.

differences in the area around the redox active cysteines C_P47/C_R166' and especially with respect to the α2-helix, in which C_P47 is located (Fig. 1). While C_P47 becomes exposed in the oxidized AhpC [9,10] due to the local unfolding of the α2-helix, resulting in an intermolecular disulfide bond with C_R166' (C_PS-SC_R), the α2-helix in the reduced state structure winds to its fully folded conformation, moving C_P47 and C_R166' more than 10 Å apart and the sulfurs to opposite directions (Fig. 1) [9–11]. During hydroperoxide decomposition, C_P47 is oxidized to cysteine sulfenic acid, which leads to local unfolding of the active site at C_P47. This in turn converts the C_P loop to be exposed to the resolving cysteine C_R166', and leads to condensation with release of water to form an intermolecular disulfide bond. The different redox states of the recently described human peroxiredoxin 4 (Prx4) reveal the formation of a Cys-SOH after H_2O_2-binding, followed by unraveling of the first turn of helix α2 to form a disulfide with the resolving cysteine from the second Prx4, which was initially about 13 Å away [12].

AhpCs are reported to undergo a redox-sensitive dimer–decamer transition, in which the oxidized protein favors catalytic dimers while the reduced AhpC preferentially assembles as five catalytic dimers in a doughnut-like feature [10]. Local unfolding in the region of the active site correlates with disulfide bond formation and structural rearrangements in the oligomeric interface, promoting dimer formation [13,14]. The decameric structure also has a stabilizing effect on the active site loop–helix (α2) with the dimer–dimer interface acting to buttress this flexible region [10,15]. Upon local unfolding in the active site loop–helix and formation of the disulfide bond, the dimer–dimer interface is perturbed, favoring dissociation of the decamer into dimers and collapse of the loop into the active-site pocket vacated by the peroxidatic cysteine [10,11,15]. The dynamics between dimers and decamers was also influenced by phosphorylation [16], protein concentration [10], pH [17] and ionic strength [18].

As indicated above, the structural insights into reduced and oxidized forms of AhpC have shed light on the events at the catalytic center. However, in crystal structures of the disulfide-bonded AhpCs, the C-terminal arm is disordered beyond the resolving cysteine, making a comparison of the C-terminus in the oxidized and reduced state of AhpC impossible. As shown in the reduced *S. typhimurium* AhpC(C47S) mutant structure the extreme C-terminus is extended and clamps around the catalytic dimer interface with its AhpC-partner, enabling residues L169, A168, G185, K186 and I187 to form polar interactions with residues of its dimeric AhpC-partner. The aim of the study presented here was to investigate the role of the very C-terminus of the AhpC enzyme and to identify critical residues important for decamer formation of reduced *Ec*AhpC. To this end, we have generated different C-terminal truncations of the 187 amino acid *E. coli* AhpC (*Ec*AhpC), called $AhpC_{1-172}$, $AhpC_{1-177}$, $AhpC_{1-182}$, $AhpC_{1-185}$ and $AhpC_{1-186}$ as well as the *Ec*AhpC mutations *Ec*AhpCK186A and *Ec*AhpCI187G. In addition, we determined the crystallographic structures of *Ec*$AhpC_{1-172}$ and *Ec*$AhpC_{1-182}$, providing additional insights into the peptide 168AKW170 which follows the resolving peptide and demonstrating for the first time that the very C-terminus of the oxidized AhpC becomes exposed and oriented away from the catalytic redox-center. Based on the importance of the C-terminus in dimer–decamer transition, we investigated the link between decamer formation, catalysis and AhpC–AhpF formation, showing that the very C-terminus of AhpC is essential for AhpC–AhpF assembly and catalysis.

2. Materials and methods

2.1. Cloning and overexpression of truncated E. coli AhpC and EcAhpC-mutant forms

The coding region for the *E. coli* C-terminally truncated constructs $AhpC_{1-172}$, $AhpC_{1-177}$, $AhpC_{1-182}$, $AhpC_{1-185}$ and $AhpC_{1-186}$, (UniProt accession number: P0AE08) was amplified by polymerase chain reaction (PCR) using forward primers 5′-CATG**CCATGG**CAATGTCCTTGATTAACA CC-3′ with a NcoI restriction site (bold) and the reverse primers 5′-GC**GAGCTC**GTTAGATTTTACCAACCAGGTC-3′ for $AhpC_{1-172}$ and 5′-GC**GAGCTC**GTTATTCTTTCCATTTAGCCGG-3′ for $AhpC_{1-172}$, 5′-GC**GAGC TC**TTACAGAGTTGCTTCACCTTC-3′ for $AhpC_{1-177}$, 5′-GTT**GAGCTC**TTAG TCCAG AGACGGAGCCAG-3′ for $AhpC_{1-182}$, 5′-GC**GAGCTC**TTAACCAACC AGGTCCAGAGAC-3′ for $AhpC_{1-185}$ and 5′-GC**GAGCTC**GTTATTTACCAA CCAGGTCCAG-3′ for $AhpC_{1-186}$ with a SacI restriction site (bold), respectively. The amplified products were ligated into the pET9-d1-His6 vector [19]. The coding sequences for all constructs were verified by DNA sequencing. The final plasmids were subsequently transformed into *E. coli* BL-21 (DE3) cells (Stratagene). To express the respective proteins, liquid cultures were shaken in LB medium containing kanamycin (30 μg/ml) for about 6 h at 310 K until an optical density OD_{600} of 0.6–0.7 was reached. To induce the production of proteins, cultures

were supplemented with isopropyl β-D-1-thiogalactopyranoside (IPTG) to a final concentration of 1 mM, followed by incubation for 4 h at 310 K.

The *Ec*AhpCK186A and *Ec*AhpCI187G-mutants have been introduced using the following PCR primers: Forward 5′-CAT G**CC ATG G**CA ATG TCC TTG ATT AAC ACC-′3 and the reverse 5′-GT **GAG CTC** TTA GAT TGC ACC AAC CAG GTC CAG-′3 for the *Ec*AhpCK186A-mutant, and 5′-CAT G**CC ATG G**CA ATG TCC TTG ATT AAC ACC-′3 (forward) as well as 5′-GC **GAG CTC** TTA ACC TTT ACC AAC CAG GTC CAG-′3 (reverse) for the *Ec*AhpCI187G-mutant.

2.2. Protein purification

E. coli cells containing recombinant *E. coli* AhpC, $AhpC_{1-172}$, $AhpC_{1-177}$, $AhpC_{1-182}$, $AhpC_{1-185}$ and $AhpC_{1-186}$ as well as the AhpCK186A and AhpCI187G-mutant proteins were harvested from 1 l cultures by centrifugation at 8000 ×*g* for 10 min at 279 K. The cells producing the respective recombinant protein were lysed on ice by sonication with an ultrasonic homogenizer (Bandelin, KE76 tip) for 3 × 1 min in buffer A (50 mM Tris–HCl pH 7.5, 200 mM NaCl, 2 mM PMSF, 1 mM Pefabloc^{SC}, 0.8 mM DTT) and buffer B (50 mM Tris–HCl pH 8.5, 200 mM NaCl, 2 mM PMSF, 1 mM Pefabloc^{SC}, 0.8 mM DTT), respectively. After sonication, the cell lysate was centrifuged at 10,000 ×*g* for 35 min at 277 K. The resulting supernatant was passed through a filter (0.45 μm; Millipore) and supplemented with Ni^{2+}-NTA resin pre-equilibrated in respective buffers. The His-tagged proteins were allowed to bind to the matrix for 1.5 h at 277 K by mixing on a sample rotator (Neolab). To avoid remaining DTT from the lysis buffer A and B, the Ni^{2+}-NTA was initially washed with 10 column volumes of respective buffers without DTT and subsequently eluted with an imidazole gradient (0–500 mM). Fractions containing the required proteins were identified by SDS-PAGE [20], pooled and concentrated using a Millipore spin concentrator with a molecular-mass cutoff of 10 kDa. The samples were applied onto an anion exchange column Resource Q (6 ml, GE healthcare), concentrated and further purified by gel filtration chromatography using a Superdex 75 HR 10/30 column (GE Healthcare) as described recently [9]. The final purity and homogeneity of the protein samples were analyzed by SDS-PAGE [20] and the gels were stained with Coomassie Brilliant Blue G250. Protein concentrations were determined by the bicinchoninic acid assay (BCA; Pierce, Rockford, IL., USA).

The *E. coli* N-terminal domain (*Ec*NTD) was produced and purified according to Dip et al. [9].

2.3. CryoEM image collection and processing

For cryoEM image collection, 2.5 μl (1 mg/ml) of reduced *Ec*AhpC and $EcAhpC_{1-172}$, respectively was applied onto C-Flat Holey Carbon Grids and subsequently blotted with filter paper for 1 s to reduce excess buffer before flash-frozen in liquid ethane at 170 K using the FEI Vitrobot Mark IV plunger. Image acquisition was performed on FEI Titan Krios electron microscope operating at 300 kV at liquid nitrogen temperature with a nominal magnification of 75,000 and an electron dose of 20–25 e/Å^2. The images were recorded on a 4096- by 4096 FEI Falcon direct electron detector. After calibration, the image pixel size was determined to be 1.14 Å. In total, 54 images were collected. Individual AhpC particle was selected semi-automatically, aided by the e2boxer tool, in Swarm mode, from EMAN2 [21] software package. A total of 1183 particles were selected for image reconstruction. The defocus for each micrograph was estimated with EMAN2 and was in the range between 2 and 6 μm underfocus. Initial model was built using EMAN2 software and refinements were performed using multi-path simulated annealing (MPSA) software assuming D5 symmetry [22]. CryoEM micrographs for reduced $EcAhpC_{1-182}$ and *Ec*AhpCI187G were collected on FEI Tecnai Arctica electron microscope operating at 200 kV at liquid nitrogen temperature with a nominal magnification of 75,000 and an electron dose of 20–25 e/Å^2. Images were recorded on a 4096- by 4096 FEI Falcon 2 direct electron detector. After calibration, the image pixel size was determined to be 2 Å. 295 and 945 particles of reduced $EcAhpC_{1-172}$ and of the *Ec*AhpCI187G mutant, respectively, were selected using EMAN2 [21] for 2D class averaging of reduced $EcAhpC_{1-172}$ and the *Ec*AhpCI187G mutant, respectively. The final geometry of the *Ec*AhpC cryoEM structure was checked, compared to the *E. coli* AhpC crystal structure and Figure was created using Chimera software [23].

2.4. Crystallization of $EcAhpC_{1-172}$ and $EcAhpC_{1-182}$

The purified C-terminally truncated $EcAhpC_{1-172}$ and $EcAhpC_{1-182}$ were concentrated to 8 mg/ml in buffer containing 50 mM Tris–HCl pH 8.5, and 200 mM NaCl, respectively by using 10 kDa cutoff concentrator. Initial crystallization screening for both proteins was carried out by the hanging-drop vapor diffusion method at 291 K using Crystal Screen 1 and 2 from Hampton Research, USA [24] and Wizard I and II (Emerald Biosystems, Inc, USA) in 48-well VDX plates (Hampton Research, USA). Initial crystallization screening of $EcAhpC_{1-172}$ yielded crystals within 2 days in Hampton crystal Screen 2 condition No. 25 (1.8 M ammonium sulfate, 100 mM MES (2- (*N*-morpholino) ethanesulfonic acid), pH 6.5 and 10 mM cobalt chloride). For $EcAhpC_{1-182}$, better quality crystals were obtained under slightly modified conditions by using 2.0 M ammonium sulfate, 100 mM MES (2- (*N*-morpholino) ethanesulfonic acid), pH 6.5.

2.5. Data collection and structure determination of $EcAhpC_{1-172}$ and $EcAhpC_{1-182}$

The crystals of $EcAhpC_{1-172}$ and $EcAhpC_{1-182}$ were quick-soaked in a cryoprotectant solution containing 25% glycerol in mother liquid and flash-cooled in liquid nitrogen at 100 K. A single wavelength dataset for $EcAhpC_{1-172}$ was collected at the protein crystallography beamline S06 PX at the Swiss Light Source (SLS) with a PILATUS 6 M detector. Data were collected as a series of 0.2° oscillation images with 0.2 s exposure time and a detector distance of 500 mm. The $EcAhpC_{1-182}$ data set was collected at 140 K in beamline 13B1 at the National Synchrotron Radiation Research Center (NSRRC, Hsinchu, Taiwan) using the ADSC Quantum 315 CCD detector. All diffraction data were indexed, integrated and scaled using the iMosflm program [25]. The results of data processing and data statistics for $AhpC_{1-172}$ and $AhpC_{1-182}$ are summarized in Table 1. The structures of $AhpC_{1-172}$ and $AhpC_{1-182}$ were solved by molecular replacement method using the entire *Ec*AhpC structure (accession code 4O5R; [9]) as model by the program PHASER [26]. Refinement was done until convergence and the geometry of the final model was validated with PROCHECK [27]. The Figure was drawn using the program PyMOL [28] and structural comparison analysis was carried out by using the SUPERPOSE program [29] as included in the CCP4 suite. The coordinates of $EcAhpC_{1-172}$ and $EcAhpC_{1-182}$ have been deposited in the Protein Data Bank (PDB ID code: 4QL7 and 4QL9).

2.6. Dynamic light scattering

Dynamic light scattering (DLS) of the reduced form of *Ec*AhpC-WT and $EcAhpC_{1-172}$ was carried out using Malvern Zetasizer Nano ZS spectrophotometer. DLS were measured in low-volume quartz batch cuvette (ZEN2112, Malvern Instruments) using 12 μl of 1 mg/ml of respective protein solution equilibrated with desire buffer solution. After 60 s equilibration time, the backscattering at 173° was detected for all proteins. To calculate the hydrodynamic diameter (D_H), size, and volume distribution, scattering intensities were analyzed by using the instrument software.

2.7. NADH dependent peroxidase activity

The NADH dependent peroxidase assay was monitored at 340 nm following the decrease in NADH absorbance. The assay was carried out

Table 1
Data collection, processing and refinement statistics for *E. coli* $AhpC_{1-172}$ and $AhpC_{1-182}$.

	Ec$AhpC_{1-172}$	*Ec*$AhpC_{1-182}$
Wavelength (Å)	1.000	1.000
Crystal-to-detector distance (mm)	500	420
Rotation range per image (°)	0.2	0.5
Total rotation range (°)	100	130
Exposure time per image (s)	0.2	15.0
Space group	$P3_121$	$P3_121$
Unit cell parameters (Å,°)		
a=	137.13	136.90
b=	137.13	136.90
c=	145.27	147.80
γ=	120	120
Molecules in asymmetric unit	5	5
Solvent content (%)	69.9	68.0
Resolution limits (Å)	30.0–3.75 (3.95–3.75)[a]	30.0–3.40 (3.52–3.40)[a]
No. of reflections	84510	175162
Unique reflections	16581	22425
Multiplicity	5.1 (5.3)	7.8 (8.0)
Completeness (%)	99.8 (100.0)	99.8 (100.0)
R_{merge}[b] (%)	5.8 (50.5)	6.6 (46.8)
$<I//\sigma(I)>$	14.6 (3.2)	19.1 (3.8)
Refinement statistics		
R-factor[c] (%)	27.31	21.21
R-free[d] (%)	28.97	23.50
Ramachandran statistics		
Favored region (%)	95.6	96.9
Allowed region (%)	4.1	2.2
Outlier region	0.2	0.9
R.M.S. deviations		
Bond lengths (Å)	0.004	0.004
Bond angles (°)	0.747	0.712
Overall B values		
Mean B value	78.1	55.2

[a] Values in parentheses refer to the corresponding values of the highest resolution shell.
[b] $R_{merge} = \Sigma\Sigma_i|I_h - I_{hi}| / \Sigma\Sigma_i I_h$, where I_h is the mean intensity for reflection h.
[c] R-factor $= \Sigma||F_O| - |F_C|| / \Sigma|F_O|$, where F_O and F_C are measured and calculated structure factors, respectively.
[d] R-free $= \Sigma||F_O| - |F_C|| / \Sigma|F_O|$, calculated from 5% of the reflections selected randomly and omitted during refinement.

at 25 °C in a total volume of 100 μl containing 300 μM of NADH, 1 mM of hydrogen peroxide and 50 mM of phosphate buffer at pH 7.0, containing 100 mM of ammonium sulfate, 0.5 mM EDTA and 1 μM of both *E. coli* AhpC and AhpF. The NADH was added finally in the reaction mixture to record the turnover rate. The NADH turnover only in the presence of AhpF alone was taken as a control. The NADH oxidation activity measured in the presence of AhpC is saturated at 6 min. The NADH oxidation was measured for both AhpF and AhpC, its truncated and mutant forms with multi-wavelength scanning ranging from 280 to 540 nm at two different time scales. The first measurement was carried out immediately after all the reaction ingredients were added and the second measurement was done after 6 min, when the NADH oxidation is saturated for AhpC.

2.8. The interaction of the AhpC C-terminus with the AhpF N-terminal domain

The effect of the *Ec*AhpC C-terminus in NTD interaction was investigated by FCS with the truncated *Ec*$AhpC_{1-172}$ and the N-terminal domain (*Ec*NTD) of *Ec*AhpF, which was fluorescently labeled by an Atto647-NHS ester (ATTO-TEC, Siegen/Germany). Prior to labeling a buffer-exchange was performed three times in a 3 kDa cutoff centrifugal filter device (Millipore). The labeling of *Ec*NTD was performed in 25 mM Hepes buffer, pH 8.1 with 150 mM NaCl for 10 min at room temperature. To remove the excess dye the diluted sample was purified by a size exclusion column (Superdex 75 HR 10/30; GE Healthcare), using 50 mM Tris–HCl pH 7.5, and 200 mM NaCl. The labeled *Ec*NTD was further on concentrated. The labeling efficiency determined by Biospec-nano Spectrophotometer (Shimadzu) was about 85%. During the experiments the temperature was set in an incubation chamber (Zeiss) to 25 °C. Increasing amounts of *Ec*$AhpC_{1-172}$ have been added, respectively. The 488 nm laser line of a 30 mW argon ion laser with following filter sets was used: MBS: HFT 488, EF: None, DBS: Mirror, and EF2: LP505 (pinhole: 90 μm). The 15 μl droplet was equilibrated on gelatin pre-treated Nunc 8-well chambered cover glass for about 3 min as described in Hunke et al. [30] [30]. Solutions of Atto647-NHS ester in Tris buffer were used as references for the calibration of the ConfoCor 3 system. The standard autocorrelation two-diffusion-coefficient normalized triplet model was used for fitting (FCS-LSM software, ConfoCor 3, Zeiss) to analyze the autocorrelation functions of *Ec*NTD bound to *Ec*$AhpC_{1-172}$. The diffusion time of fluorescently labeled *Ec*NTD was measured independently, and kept fixed during the fitting of the FCS titration data. The determination of the binding constants required the calculation of the relative amounts of free labeled *Ec*NTD with the short diffusion time versus the diffusion time of the larger complex of the non-labeled protein with *Ec*NTD. The calculations of the bound fractions and the dissociation constants were done as described above.

3. Results

3.1. Ring formation of E. coli AhpC under reduced conditions

The recently determined crystal structure of the oxidized *E. coli* AhpC (*Ec*AhpC) reveals that five molecules (A–E) in the asymmetric unit form a half-ring conformation and a decameric ring *Ec*AhpC is generated by its crystallographic two-fold symmetry operation (A′–E′) [9]. In order to prove the presence of decameric rings in physiological and reduced conditions cryoEM images of the reduced *Ec*AhpC were collected. Images of the reduced *Ec*AhpC showed high amounts of ring-like and also rod-shaped particles, likely representing the top and side views of the ring structure, respectively (Fig. 2A). A total of 54 images were collected and 1183 isolated particles were selected for averaging into 40 different classes (Fig. 2B). The class averages revealed the length of the rod-shaped particles of approximately 140 Å, which is consistent with the 124 Å diameter of the crystallographic *Ec*AhpC-decamer [9]. This indicates that the rod-shaped particle reflects the side-view of the ring-shaped *Ec*AhpC-particle. Single-particle reconstruction (SRP) of the reduced *Ec*AhpC was performed with the 18 best-generated classes in different perspectives for initial model building using EMAN2 software [21] (Fig. 2C). The EMAN2 software uses the class averages to build a set of initial 3D-models for SPR. The initial model in the reduced form was used as a template for refinement by assuming D5 symmetry in the 3D-reconstruction using MPSA software [22]. The asymmetric unit of D5 is defined in terms of the 5-fold and 2-fold axes of symmetry. After ~35 iterations, the cryoEM map refinement converged. The final map resolution was 12.2 Å as estimated using Fourier shell correlation of independent half-data sets, with a cutoff at 0.5 (Supplemental Fig. 1). A cryoEM map of the reduced *Ec*AhpC shows a ring shape conformation with a dimension of 130 × 130 × 45 Å (Fig. 2C). The inner and outer diameter of the ring is 40 Å and 130 Å, respectively (Fig. 2C). The ring structure reveals a five-fold symmetry reflected by five oval shaped segments (Fig. 2D) that are separated by narrow gaps. The top view of the ring showed at least four small protruding densities that are projecting out of each segment (Fig. 2E). The side-view reveals a rod-shape conformation, highlighting that small protrusions are present on both sides of the ring formation (Fig. 2F). Each of the segments has a dimension of 70 × 45 × 45 Å and reflects an additional two-fold axis, dividing the segment into two regions (Fig. 2E, left). The top view of one segment reveals that each region has three small protrusions on one side and two on the other side (Fig. 2E, right). The comparison of the cryoEM map and *Ec*AhpC crystal structure in the oxidized form [9] highlights similar shape and dimension for both structures (Fig. 2F), reflected by a correlation coefficient of 0.91 as calculated using the Chimera program (Fig. 2F). Each of the five oval shaped segments of

the reduced cryoEM map corresponds to two AhpC monomers (Fig. 2F). The superposition of one oval shape segment and the crystal structure of oxidized *Ec*AhpC reveal that the oval shape segment has larger dimension than the corresponding oxidized crystal structure (see arrows in Fig. 2F).

3.2. The extreme C-terminus in the reduced EcAhpC is essential for decamer assembly

The very C-terminal residues in the reduced state of the *S. typhimurium* AhpC(C47S) mutant structure move closer to the dimer interface and bring residues L169 and A168 to amino acids R143′ and T49′ of the neighboring AhpC, respectively [10]. In addition, residues G185, I187 and I187 in the reduced form are in proximity to residues F43′, P48′, T88′ as well as S86′ of the second AhpC, respectively (Fig. 3). In order to investigate the role of the C-terminus in decamer assembly, we generated the recombinant C-terminal truncated forms $AhpC_{1-172}$ and $AhpC_{1-182}$ of *Ec*AhpC. Both proteins could be prepared to high purity and have been used for single particle analysis. Cryo-electron micrographs of reduced *Ec*$AhpC_{1-172}$ and *Ec*$AhpC_{1-182}$ are shown in raw images in Fig. 4A–B and Supplemental Fig. 3, respectively. In contrast to the reduced *Ec*AhpC-WT, no ring-shaped particles were observed in the electron micrographs of the reduced *Ec*$AhpC_{1-172}$ or *Ec*$AhpC_{1-182}$ proteins. A total of 295 particles of the reduced *Ec*$AhpC_{1-172}$ were subjected to image processing. Fig. 4B demonstrates that mostly small round particles with a width of about 70 Å were obtained for the reduced *Ec*$AhpC_{1-172}$. To confirm the change in oligomeric state assembly of the reduced *Ec*AhpC-WT and *Ec*$AhpC_{1-172}$, respectively, dynamic light scattering (DLS) experiments were performed (Fig. 4C). The reduced form of *Ec*AhpC-WT and *Ec*$AhpC_{1-172}$ shows a molecular weight of 184.2 ± 48 kDa and 35.4 ± 5.1 kDa, respectively, indicating that only the reduced *Ec*AhpC-WT has the tendency to form a larger oligomer, while the reduced *Ec*$AhpC_{1-172}$ is organized as a lower molecular weight oligomer corresponding to a dimer (Fig. 4C).

To further identify the critical residue(s) involved in decamer formation, the last amino acid (I187) was mutated to glycine and a highly pure *Ec*AhpCI187G mutant protein was prepared (Supplemental Fig. 4). CryoEM images of this mutant protein were collected and

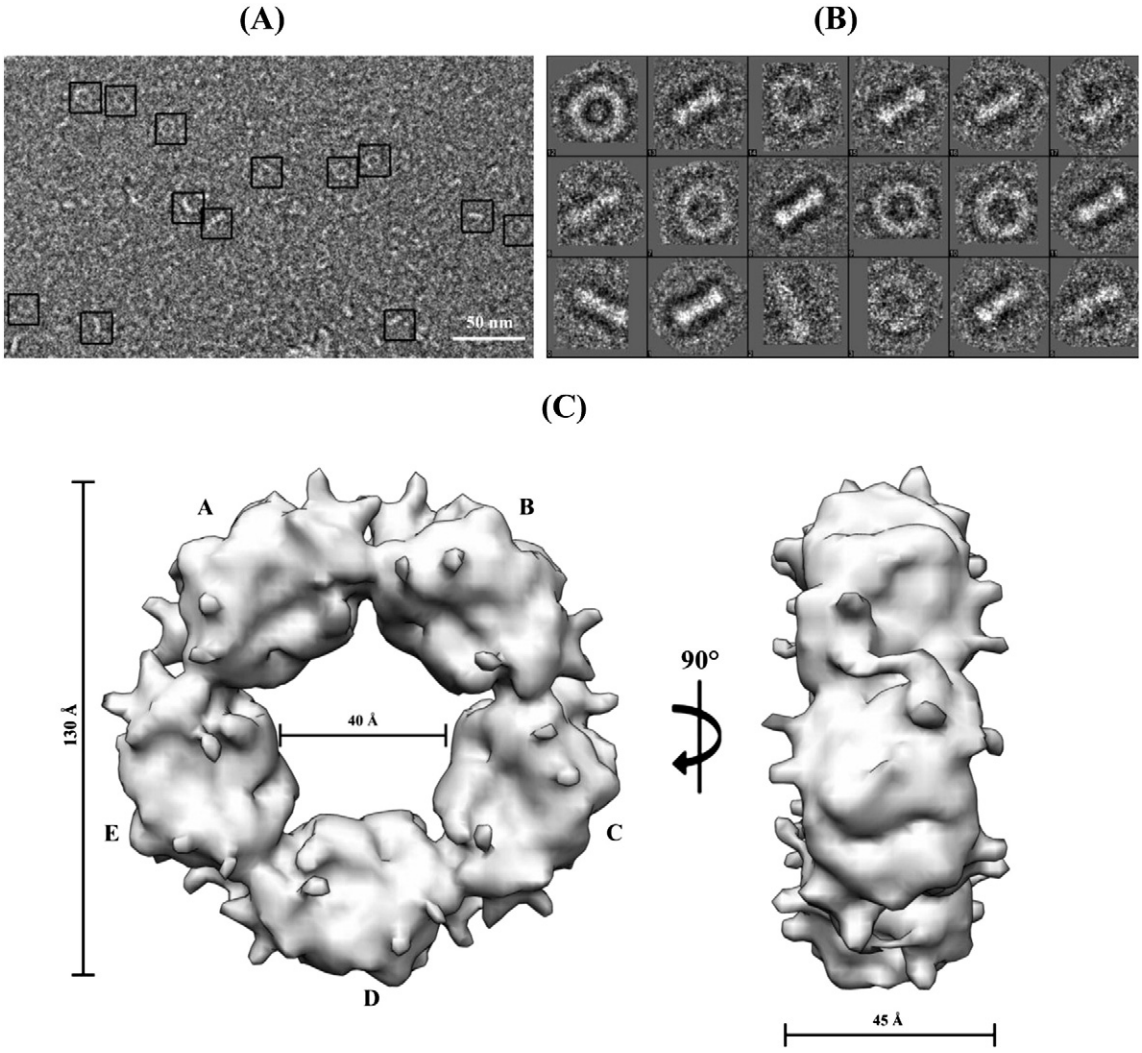

Fig. 2. CryoEM images and 3D reconstruction of *E. coli* AhpC. (A) Micrograph of *Ec*AhpC in its reduced form. Selected particles are highlighted in boxes for class averaging. The box size was selected to 192 pixels with a pixel size of 1.14 Å/pixel. (B) Selected class average images of isolated *Ec*AhpC particles in reduced form. (C) The cryoEM 3D reconstruction of *Ec*AhpC on top view reveals a ring shape conformation. The ring structure has a dimension of 130 Å × 130 Å × 45 Å and consists of five well-defined oval shaped segments labeled as A–E. The 90° view highlights a rod shape conformation. (D) Each segment reveals a 2-fold symmetry axis resulting in 10 symmetrical units within the entire *Ec*AhpC reconstruction. (E) Close-up view of one segment. Each segment has a dimension of 70 Å × 45 Å × 45 Å. The two symmetrical regions are colored blue and yellow. On the left, one segment is depicted along its two fold axis. The top view (right) reveals that each region of a segment has three small protrusions; one on one side and two on the other. (F) Structural comparison between the recently determined crystal structure (PDB ID: 4O5R) and cryoEM map of *Ec*AhpC. Fitting of the crystal structure of the oxidized form of *Ec*AhpC [9] into the cryoEM map of the reduced form reveals similar dimensions with a correlation coefficient of 0.91 [23].

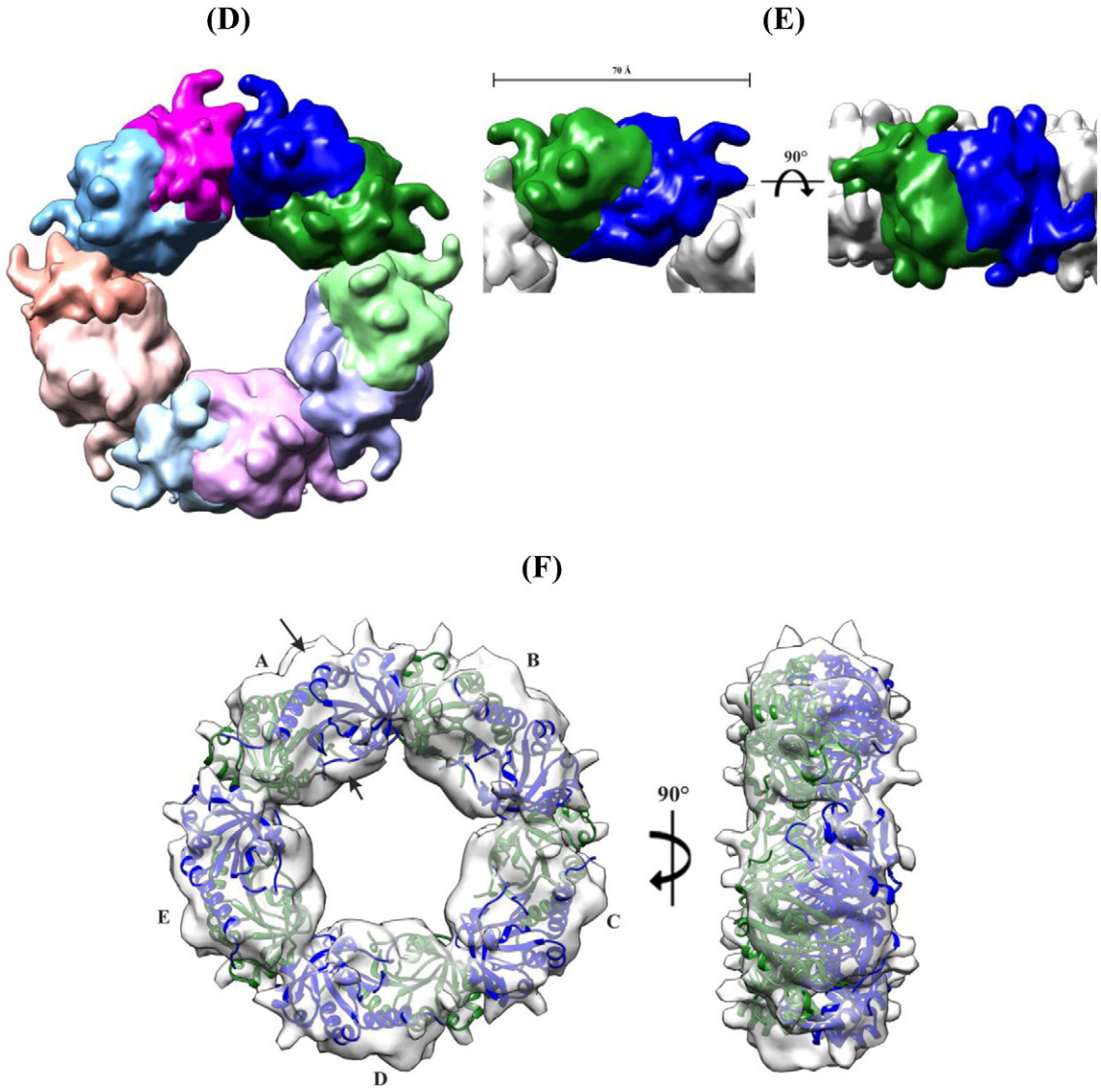

Fig. 2 (*continued*).

presented in Fig. 4D. As demonstrated in the representative micrograph and 2D projections of the *Ec*AhpCI187G mutant (Fig. 4E), no rings or rods were observed, but rather small round particles, indicating the importance of the last residue I187 in decameric ring formation.

3.3. Redox-modulated structural rearrangements of the very C-terminus of AhpC

In order to confirm that the C-terminal truncation of *Ec*AhpC$_{1\text{-}172}$ and *Ec*AhpC$_{1\text{-}182}$ does not alter the structural traits of the proteins and to get more structural insight into the extreme C-terminus of the disulfide-bound form of AhpC, both truncated versions of the protein were crystallized (Supplemental Fig. 2A–B). The crystals were of good diffraction quality and allowed us to determine the crystallographic structures of *Ec*AhpC$_{1\text{-}172}$ and *Ec*AhpC$_{1\text{-}182}$ at 3.75 Å and 3.4 Å, respectively. The results of data processing and data statistics for *Ec*AhpC$_{1\text{-}172}$ and *Ec*AhpC$_{1\text{-}182}$ are summarized in Table 1. Like for the *Ec*AhpC protein [9], both *Ec*AhpC$_{1\text{-}172}$ and *Ec*AhpC$_{1\text{-}182}$ show five molecules in the asymmetric unit and an overall decameric ring assembly, generated by its crystallographic two-fold symmetry operation (Fig. 5A, Supplemental Fig. 2C). Both of the *Ec*AhpC$_{1\text{-}172}$ and *Ec*AhpC$_{1\text{-}182}$ monomers, consists of a central seven-stranded β-sheet, flanked at one side by four and at the other side by two α-helices (Fig. 5B). Each monomer contains both the peroxidative cysteine (C_P47) and the resolving cysteine (C_R166). The dimer interface is mainly stabilized by salt bridge and hydrogen bond interactions, which are formed between β7 and β7′ of each monomer. Altogether this forms a combined 14 stranded β-sheet structure (Fig. 5B). As demonstrated in the 2Fo-Fc electron densities, the active site of AhpC is composed of the intermolecular disulfide bond between the C_P47 of one monomer and C_R166′ of the other monomer, interacting in a head to tail manner contributing to dimer assembly (Fig. 5C–D).

Superposition of the 3.3 Å *Ec*AhpC structure [9] with the corresponding dimer of *Ec*AhpC$_{1\text{-}172}$ and *Ec*AhpC$_{1\text{-}182}$ resulted in an r.m.s.d. value of 0.41 and 0.28 Å, respectively, and 0.38 Å between *Ec*AhpC$_{1\text{-}172}$ and *Ec*AhpC$_{1\text{-}182}$, indicating that the truncation at the C-terminus has not altered the structural features of the protein and in particular not the interacting epitope of the catalytically important disulfide formation between C_P47 and C_R166 (Fig. 5B). Whereas the residues 168–182 could not be resolved in the recently determined *Ec*AhpC structure [9], amino acids 168–170 could be resolved in one of the chains of the *Ec*AhpC$_{1\text{-}172}$ crystallographic structure (Fig. 5B). Residues 168AKW170 are oriented away from the neighboring AhpC molecule and away from the catalytic redox-center (Fig. 5A–B).

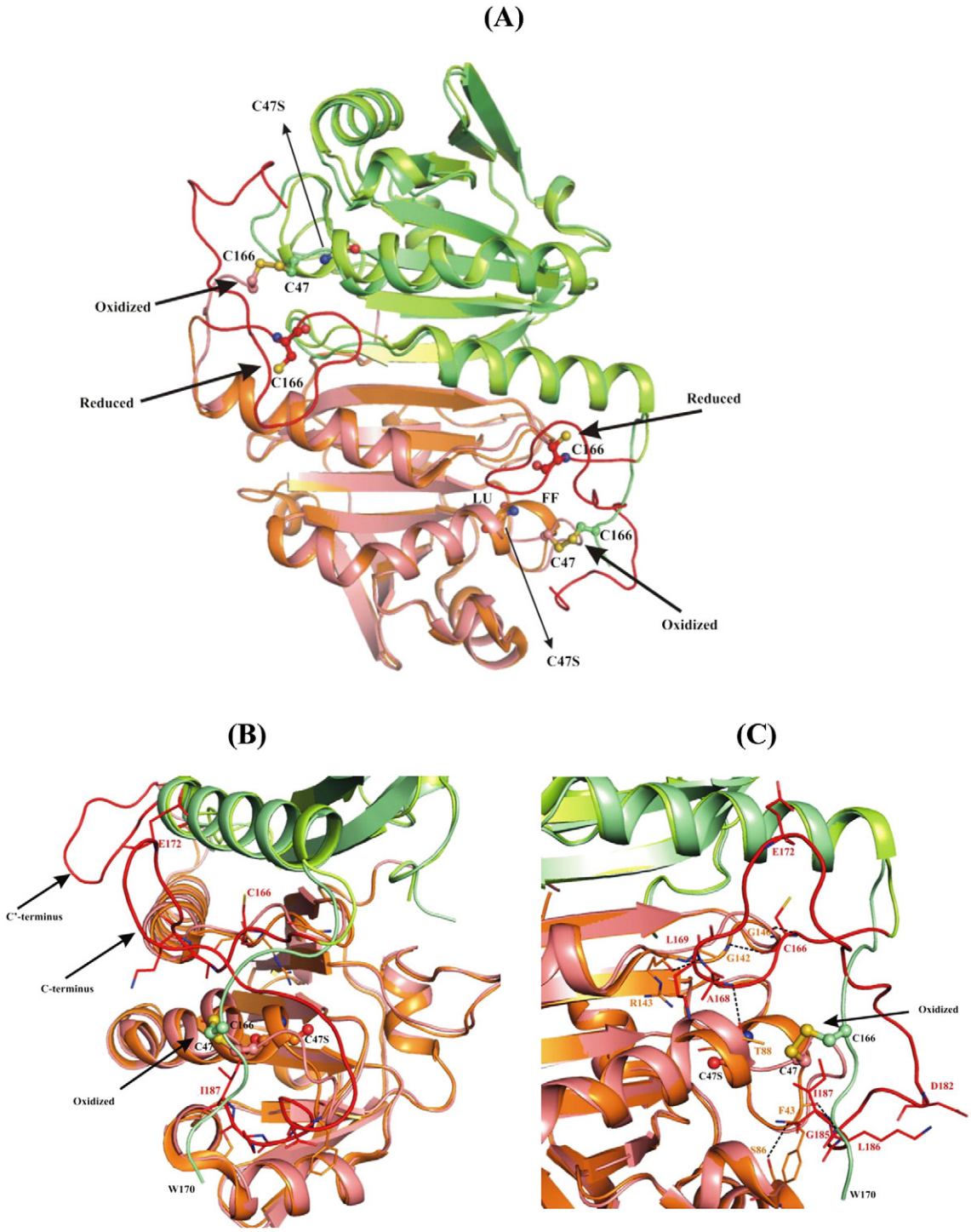

Fig. 3. Superposition of oxidized *E. coli* AhpC and reduced *S. typhimurium* AhpC crystal structures. (A) The reduced *St*AhpC crystal structure (PDB ID: 1N8J) reveals additional C-terminal residues, highlighted in red. (B) Close-up view of the disulfide bond and C-terminal region of *Ec*AhpC$_{1-172}$ and *St*AhpC, respectively. (C) C-terminal region of *St*AhpC reveals that an additional hydrogen bond with C-terminal residues stabilizes the dimer interface, while the disulfide bond interaction appears in the oxidized form with residues in the C-terminal region oriented outwards and adopting a more exposed conformation.

A comparison of the three structures of the oxidized form of *Ec*AhpC-WT, *Ec*AhpC$_{1-172}$ and *Ec*AhpC$_{1-182}$ with the *S. typhimurium* AhpC(C47S) mutant structure, representing the so-called reduced state (PDB ID: 1N8J) [11], reveals differences to the α2-helix, in which C_P47 is located (Fig. 3A–B). In the case of the oxidized *Ec*AhpC, C_P47 becomes exposed due to the local unfolding of the α2-helix, resulting in an intermolecular disulfide bond with C_R166′ (C_PS-SC_R). In contrast, in the reduced state of the *St*AhpC(C47S) mutant structure, the α2-helix is obtained in its fully folded conformation, moving C_P47 and C_R166′ more than 10 Å apart and the sulfurs to opposite directions (Fig. 3). Although the very C-terminal residue of the structures in the oxidized forms of *Ec*AhpC-WT, *Ec*AhpC$_{1-172}$ and *Ec*AhpC$_{1-182}$ of the crystal structures cannot be resolved, the residues 168AKW170 in the *Ec*AhpC$_{1-172}$ structure presented show for the first time its orientation moving away from the catalytic site, which is formed by an intermolecular disulfide bond between the C_P47 of one monomer with C_R166′. That would indicate that the very

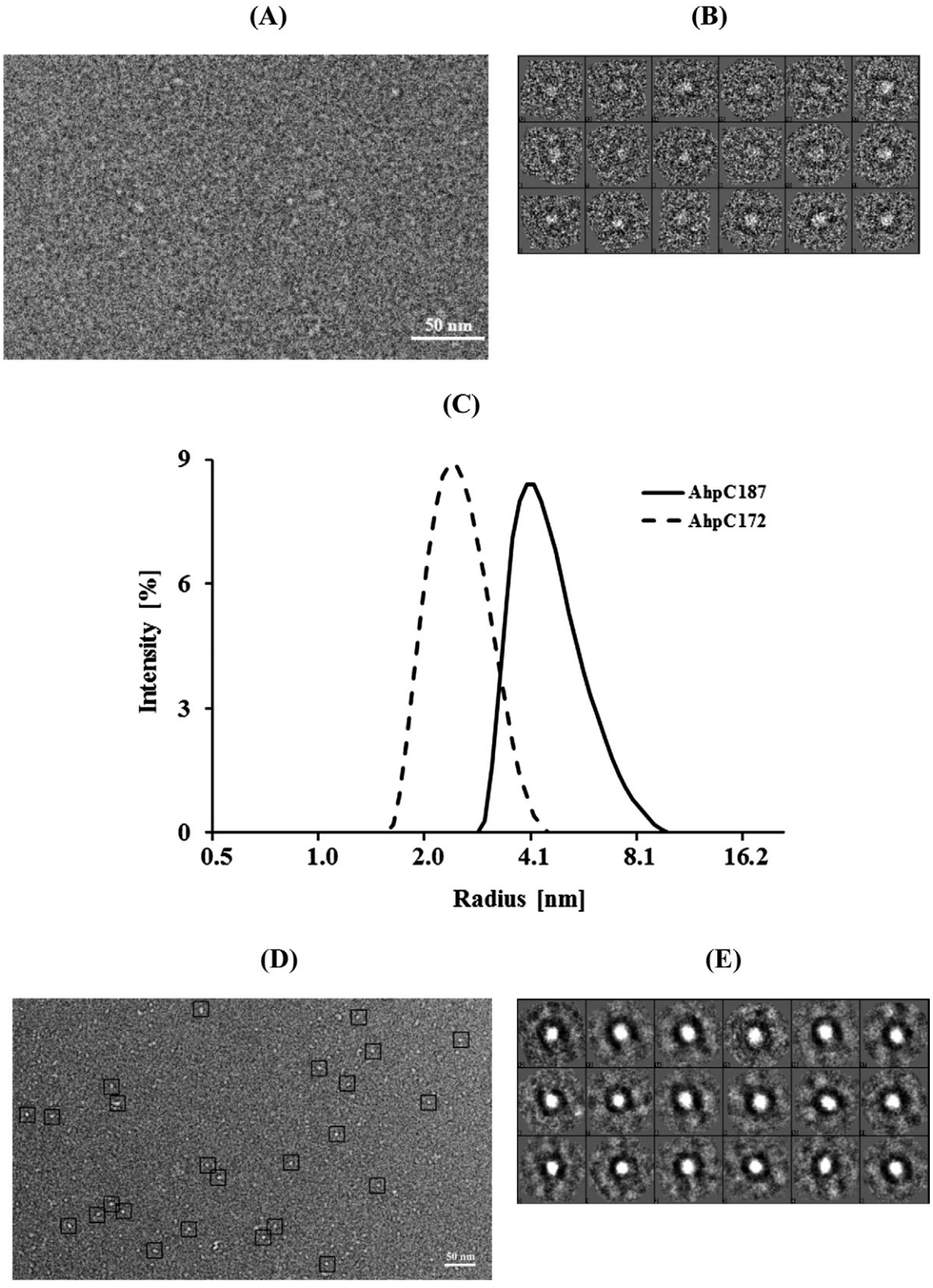

Fig. 4. Cryo-EM images of *Ec*AhpC$_{1\text{-}172}$ and the mutant *Ec*AhpCI187G. (A) Micrograph of *Ec*AhpC$_{1\text{-}172}$ in its reduced form. Ring and rod shape particles were not found; rather small round particles with a dimension of about 70 Å were selected for (B) 2D class averaging using EMAN2 software [21]. (C) Dynamic light scattering experiments of *E. coli* AhpC and *Ec*AhpC$_{1\text{-}172}$ were used to determine the hydrodynamic radius of *Ec*AhpC (—) and *Ec*AhpC$_{1\text{-}172}$ (—) in 50 mM Tris/HCl pH 7.5, 200 mM NaCl, 1 mM DTT. *Ec*AhpC and *Ec*AhpC$_{1\text{-}172}$ revealed a hydrodynamic radius of 4 nm and 2.2 nm, respectively, indicating that *Ec*AhpC$_{1\text{-}172}$ exists as smaller oligomer under reducing condition. (D) Micrograph of *Ec*AhpCI187G in its reduced form. Small round particles were found and selected for 2D class averaging. (E) 2D class averages of *Ec*AhpCI187G reveal round shape particles with a dimension of about 70 Å.

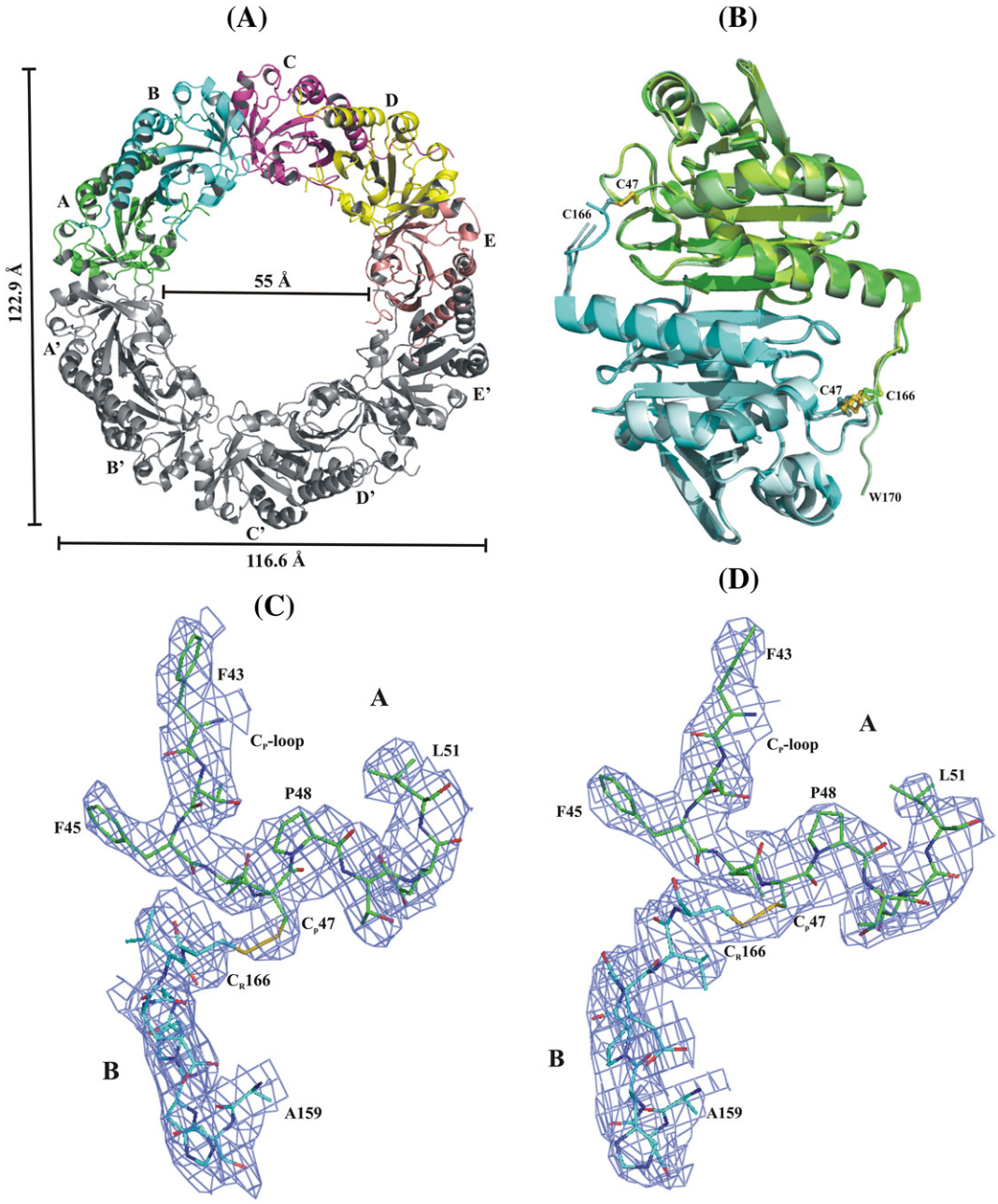

Fig. 5. Structural features of *Ec*AhpC$_{1\text{-}172}$ and *Ec*AhpC$_{1\text{-}182}$. (A) The crystal structure of oxidized *Ec*AhpC$_{1\text{-}172}$ in decameric form $(\alpha_2)_5$. Each asymmetric unit consists of five molecules depicted in different colors (A–E), and their crystallographic symmetry mates, depicted in gray (A′–E′). Dimer formations are between A and B, C and D and E and E′. (B) Superposition of the dimer of oxidized *Ec*AhpC with the truncated forms of *Ec*AhpC$_{1\text{-}172}$ and *Ec*AhpC$_{1\text{-}182}$ confirms that no significant structural modification resulted from truncations. The crystallographic *Ec*AhpC dimer-structure is colored in green and blue, while AhpC$_{1\text{-}172}$ and AhpC$_{1\text{-}182}$ is colored in brighter shades. (C) The 2Fo-Fc density map around the C_P disulfide is revealed and bonded with C_R from the dimeric partner subunit for *Ec*AhpC$_{1\text{-}172}$ contoured at 1 σ (blue lines) and for *Ec*AhpC$_{1\text{-}182}$ (D).

C-terminus becomes more exposed in the oxidized form of *Ec*AhpC. By comparison, the extreme C-terminal residues in the reduced state of the *St*AhpC(C47S) mutant move closer to the dimer interface and bring residues L169 and A168 closer to the amino acids R143′ and T49′ of the neighboring AhpC, respectively. Similarly, the residues G185, K186 and I187 in the reduced form are in the proximity of residues F43′ and P48′, T88′ as well as S86′ of the second AhpC, respectively (Fig. 3).

3.4. NADH-dependent peroxidase activity is dependent on the C-terminus of EcAhpC

The two AhpR subunits AhpF and AhpC form an enzymatically active complex which catalyzes the detoxification of hydrogen peroxide by shuttling the reducing equivalent from NADH to hydrogen peroxide. The decrease in NADH absorbance in the presence of *Ec*AhpF alone (Fig. 6A) reflects the electron transfer from NADH to the AhpF redox centers via FAD to the redox active disulfide C345/C348 of the C-terminal domain of *Ec*AhpF and further to the N-terminal C129/C132 disulfide center of the N-terminal domain of *Ec*AhpF (Fig. 6A). In the presence of *Ec*AhpC-WT, the absorbance dropped significantly and reached saturation after 6 min of the reaction (Fig. 6A; insert). The result clearly indicated that for H_2O_2 reduction and maximum NADH-oxidation both AhpF and AhpC are required. In order to compare the catalytic activity of different truncated AhpC proteins with the full length AhpC protein, the NADH oxidation was measured directly after incubation as well as after saturation (6 min)

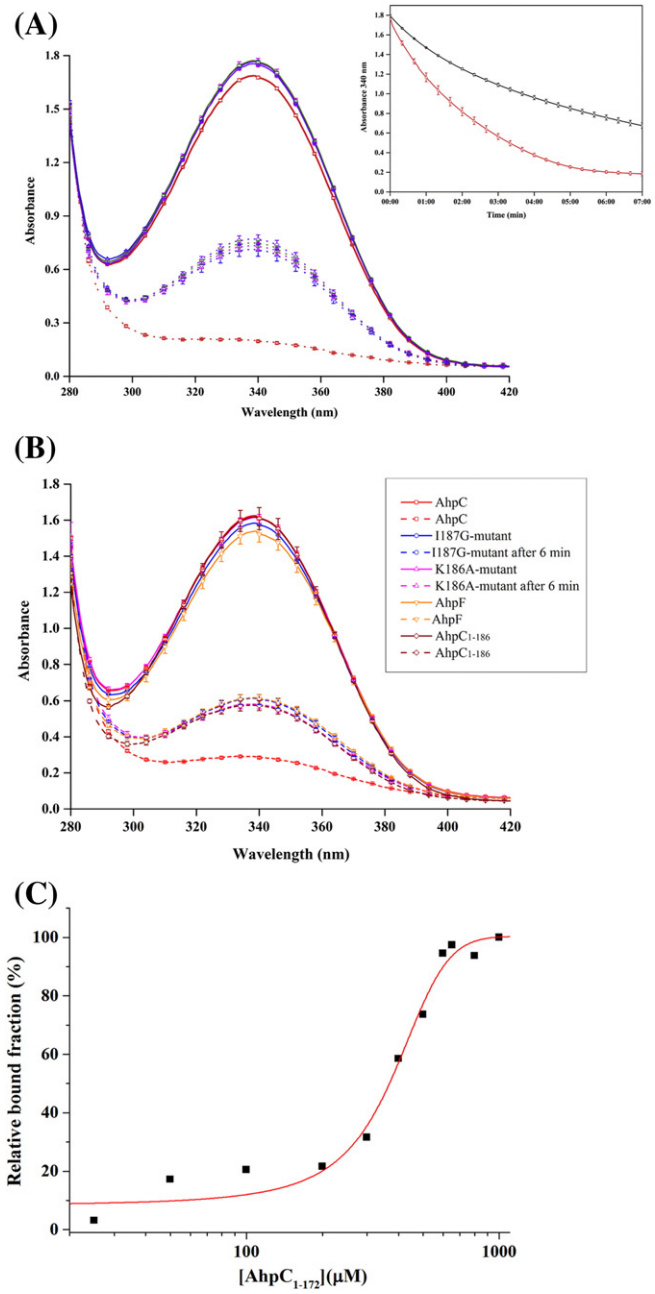

Fig. 6. NADH-dependent assay of the AhpC–AhpF complex and AhpC-NTD interaction. (A) The NADH dependent peroxidase activity was measured in the presence of *Ec*AhpC, *Ec*AhpF and H_2O_2. The insert shows catalytic activity in presence of entire *Ec*AhpC (red line) and the absence of *Ec*AhpC (black line) as a control. The data demonstrate that the NADH oxidase activity was saturated at 6 min. The NADH dependent peroxidase activity of *Ec*AhpC and the truncated proteins (*Ec*AhpC$_{1-172}$ (purple), *Ec*AhpC$_{1-177}$ (green), *Ec*AhpC$_{1-182}$ (magenta) and *Ec*AhpC$_{1-185}$ (blue)) were measured at 0 min and 6 min, respectively. In the presence of *Ec*AhpC, maximum catalytic activity was observed. Measurement taken at 0 min (continuous line) and after 6 min (dotted line) show that only the entire *Ec*AhpC protein is catalytically active. (B) The NADH-dependent peroxidase activity measured for *Ec*AhpC, the truncated *Ec*AhpC$_{1-186}$ and the mutant proteins *Ec*AhpCL186A and *Ec*AhpCI187G was observed in a range from 280 to 540 nm at 0 min and 6 min. The data presented are average of three independent measurements, and error bars represent the standard deviation. (C) Binding of *Ec*NTD to *Ec*AhpC$_{1-172}$ by fluorescence correlation spectroscopy. Concentration dependent binding traits of Atto647-labeled *Ec*NTD to *Ec*AhpC$_{1-172}$. Best fits yielding the binding constants are represented as a line fitted by a non-linear, Boltzmann curve fit.

(Fig. 6A). Maximum catalytic activity was observed in the presence of *Ec*AhpC, indicating an active AhpR complex formation. However, the spectra of the truncated *Ec*AhpC$_{1-172}$ or *Ec*AhpC$_{1-182}$ proteins resembled that of *Ec*AhpF alone (control), reflecting that no active AhpR complex was assembled. We also generated the recombinant truncated proteins of *Ec*AhpC$_{1-177}$, *Ec*AhpC$_{1-185}$ and *Ec*AhpC$_{1-186}$ (Supplemental Fig. 4). When added to the NADH-dependent peroxidase activity assay no enzymatic activity could be measured. In order to investigate the effect of individual residues of the AhpC C-terminus on enzymatic activity, the *Ec*AhpCI187G mutant as well as the *Ec*AhpCK186A mutant (Supplemental Fig. 4) were generated and studied. Similar to the truncated *Ec*AhpC proteins, substituting the very C-terminal residues K186 and I187 of *Ec*AhpC resulted in an enzymatically non-active AhpR complex (Fig. 6B).

3.5. The C-terminus of EcAhpC forms the anchor for AhpC–AhpF assembly

For the electron transfer between AhpF and AhpC, the two proteins become apposed and transiently linked via a mixed disulfide bond. Therefore, the understanding of the complex formation between the two proteins is critical. As demonstrated previously, *Ec*AhpC binds to the *E. coli* N-terminal domain (*Ec*NTD) of AhpF with a dissociation constant (K_D) of 3.2 μM [9]. In order to demonstrate the importance of the very C-terminus in AhpC–AhpF assembling, the binding of fluorescently labeled *Ec*NTD to the truncated *Ec*AhpC$_{1-172}$ has been studied. The diffusion time for Atto647N labeled *Ec*NTD bound to *Ec*AhpC$_{1-172}$ was determined to be 530 μs. The addition of non-labeled *Ec*AhpC$_{1-172}$ to the Atto647 labeled *Ec*NTD caused a change in the mean diffusion time t_D, indicating binding of the two proteins. The calculated values of the fitted autocorrelation functions were plotted as relative bound fractions versus the concentration of *Ec*AhpC$_{1-172}$ (Fig. 6C). A curve was fitted to the data points by using a non-linear Boltzmann function. The binding constant for the interaction of *Ec*AhpC$_{1-172}$ with *Ec*NTD was estimated to be 382.38 ± 25.87 μM (Fig. 6C). This demonstrates that *Ec*AhpC$_{1-172}$ binds to the *Ec*NTD with a binding constant that is more than 100-times lower than that of the entire *Ec*AhpC. This result reveals that the very C-terminus of AhpC is essential for AhpC–AhpF assembly.

4. Discussion

The oxidized AhpC can only execute its function after reduction of its cysteines to their thiol form via AhpF [1]. The presented cryoEM map as well as the light scattering experiments of the reduced *E. coli* AhpC reveal the enzyme to be a decamer composed of five catalytic dimers with each monomer having both a hydrophobic- and oligomer interface. The hydrophobic interface between chain B and chain C of the oxidized *Ec*AhpC$_{1-172}$- and *Ec*AhpC$_{1-182}$ structures (Fig. 7) and its overlay with the surface-rendered cryoEM map reveal that the hydrophobic residues F21, F43, F45, F77, A81 and W82 are accommodated by the cryoEM map of the reduced enzyme (Fig. 7). Superposition of the oxidized *Ec*AhpC$_{1-172}$- or *Ec*AhpC$_{1-182}$ structure and the reduced *St*AhpC(C47S) mutant crystal structures show (Fig. 3B), that this hydrophobic epitope, proposed to build the oligomer interface [11], seems to be without any significant structural alterations dependent upon redox modulation.

By comparison, superposition of the oxidized *Ec*AhpC [9] and reduced *St*AhpC(C47S) mutant [11] with the cryoEM map of the reduced *Ec*AhpC demonstrates that one oval shape segment is larger than the corresponding oxidized crystal structure. The C-terminal region is flexible under oxidized conditions and hence not visible in the crystal structure, whereby the additional volume in the cryoEM map of the reduced *Ec*AhpC is mainly occupied by the C-terminal region (residues 168 to 187) of the reduced *St*AhpC(C47S) mutant [11] (Fig. 7). The C-terminus of one monomer reaches across the dimer interface to the other monomer in the reduced state to hold both monomers together at the dimer interface. It can be observed that in the reduced *St*AhpC(C47S) mutant, the residues from C166 onwards form defined hydrogen bonds at two regions with their partner molecule. The first region includes residues C166, K169 and A168, forming four hydrogen bonds to G139′, G142′, R143′ and T49′, highlighted by arrows

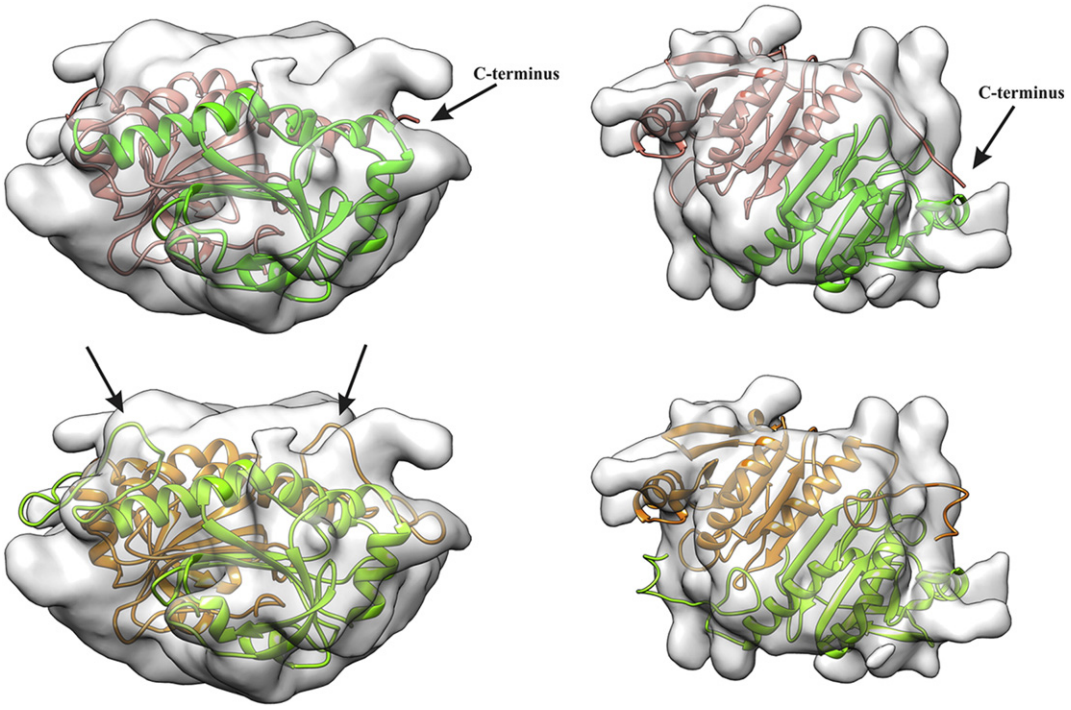

Fig. 7. The ins and outs of the AhpC C-terminus. The top row shows side (left) and top views (right) of the superposition of one oval shaped segment and two *Ec*AhpC$_{1-172}$ monomers (pink and green) in oxidized form. The lower row shows side (left) and top views (right) of the superposition to one oval shaped segment and two *St*AhpC(C47S) mutant proteins in reduced form ([10], orange and bright green). The dimensions of the cryoEM map of the reduced *Ec*AhpC are larger than the once of the oxidized *Ec*AhpC$_{1-172}$ crystal structure. The C-terminus of the oxidized *Ec*AhpC$_{1-172}$ crystal structure is projecting out of the EM density map, which is highlighted with an arrow. The superposition of the 3D reconstruction of the reduced *Ec*AhpC and the crystal structure of *St*AhpC in reduced form [10] indicate that the additional volume represents the rigid C-terminal region of the reduced structure (black arrows).

(Figs. 3A–C, 7). Interestingly, T49′ is located at the α2-helix in which C_P47 is located. The winding of the fully folded α2-helix forms an additional interface for hydrogen bonding to A168. The second region includes the residues at the extreme C-terminus, G185 and I187, which form hydrogen bonds with F43′, F45′, S86′ and T88′, respectively. In addition, I187 is in weak contact with P48′ and T49′ located at the α2-helix in the FF conformation. Significantly, residues F43′ and F45′, which interact with the very C-terminus, are the key residues building the oligomer interface in the reduced state and the interaction made by these residues are disrupted upon redox-modulated structural alteration and hence lead to the destabilization of the decamer [10]. The elimination of these C-terminal residues as in the reduced *Ec*AhpC$_{1-172}$ and *Ec*AhpC$_{1-182}$ or even substitution of residue I187 in the reduced *Ec*AhpCI187G mutant protein clearly prevented the formation of decameric rings as demonstrated in our cryoEM images (Fig. 4A–E). These data reveal for the first time the importance of hydrogen bond formation between the AhpC C-terminus and its partner for decamer formation.

This model is supported by the crystallographic structure of the oxidized *Ec*AhpC$_{1-172}$ C-terminus, in which the C-terminus is oriented above two neighboring AhpC molecules, faces to the outside of the dimer-interface (Fig. 7), and is exposed so as to enable the binding to the N-terminal domain of AhpF (*Ec*NTD). This reorientation of the C-terminus in the oxidized protein prevents AhpC to form hydrogen bonding with its second dimerization partner, likely to influence the stability of the oligomeric interface, which mainly relies on the hydrophobic epitope composed of residues F21, F43, F45, F77, A81 and W82 (see above). So far, it has been postulated that the peroxidatic cysteine (C_P47) is exposed in the oxidized AhpC [9,10] due to the local unfolding of the α2-helix, leading to an intermolecular disulfide bond with C_R166′ (C_PS-SC_R). The data presented here raise the question as to whether it is the unwinding of the C-terminus in the oxidized AhpC which triggers the intermolecular disulfide formation. That would allow the very C-terminus, which is described here to be more exposed and accessible for the AhpF, to bind and consequently facilitate the electron transfer from the $_{129}$CXXC_{132} motif in the NTD to the C_PS-SC_R of AhpC.

Most recently, we have shown that *Ec*AhpC and *Ec*AhpF interact via the N-terminal domain of *Ec*AhpF with a moderate K_D of 3.2 μM [9]. The more than 100-times lower binding of the NTD of *Ec*AhpF and the truncated *Ec*AhpC$_{1-172}$ is nicely in line with a model in which the AhpC C-terminus is exposed and the binding epitope is responsible for the *Ec*AhpC–*Ec*AhpF complex formation. The NADH-dependent peroxidase measurements of the truncated forms of *Ec*AhpC$_{1-172}$, *Ec*AhpC$_{1-177}$, *Ec*AhpC$_{1-182}$, *Ec*AhpC$_{1-185}$ and *Ec*AhpC$_{1-186}$ as well as the *Ec*AhpC mutant proteins *Ec*AhpCK186A and *Ec*AhpCI187G confirm that the very C-terminus of AhpC is important for both the NADH-dependent peroxidase activity of the AhpC–AhpF complex as well as for complex assembly. In our study, the decameric ring formation of reduced His6×-tag *Ec*AhpC under more physiological conditions, like in the cryoEM- and light scattering studies, is nicely complemented by the recent investigation, suggesting that the His-tag has no significant influence on oligomerisation [31]. Furthermore, it has been reported that the presence of the related His-tagged *At*-PRX shows a failure of enzymatic saturation compared to the His-tagged free form [32]. In our study, the His-tagged *Ec*AhpC revealed a saturation after 6 min, indicating that the tag did not effect the catalytic efficiency of the enzyme.

It has been reported that the application of antimycobacterial drugs to *Mycobacterium tuberculosis* strains results in a drastic decrease of AhpC activity; however, the mechanistic basis for this phenomenon remains unclear [33]. Insights into the role and mechanism(s) of the AhpC C-terminus presented here suggest mechanisms by which this may occur, and point to a promising target for the development of novel therapeutics.

Acknowledgements

This study was supported by the School of Biological Sciences (SBS) and Nanyang Technological University (NTU); New Initiative Fund FY

2010 (to GG). Phat Dip is grateful to receive the Singapore International Graduate Award (SINGA). We thank Dr. S. Bhushan and Dr. A. Wong at SBS for their great help in collecting EM-images. We thank Professor M. Featherstone, School of Biological Sciences, NTU, for critically reading the manuscript.

Appendix A. Supplementary data

Supplementary data to this article can be found online at http://dx.doi.org/10.1016/j.bbabio.2014.08.007.

References

[1] A. Hall, K. Nelson, L.B. Poole, P.A. Karplus, Structure-based insights into the catalytic power and conformational dexterity of peroxiredoxins, Antioxid. Redox Signal. 15 (2011) 795–815.
[2] C.C. Winterbourn, Reconciling the chemistry and biology of reactive oxygen species, Nat. Chem. Biol. 4 (2008) 278–286.
[3] A.G. Cox, C.C. Winterbourn, M.B. Hampton, Mitochondrial peroxiredoxin involvement in antioxidant defence and redox signalling, Biochem. J. 425 (2009) 313–325.
[4] A.J. Link, K. Robison, G.M. Church, Comparing the predicted and observed properties of proteins encoded in the genome of *Escherichia coli* K-12, Electrophoresis 18 (1997) 1259–1313.
[5] L.A. Tartaglia, G. Storz, B.N. Ames, Identification and molecular analysis of oxyR-regulated promoters important for the bacterial adaptation to oxidative stress, J. Mol. Biol. 210 (1989) 709–719.
[6] L.B. Poole, H.R. Ellis, Flavin-dependent alkyl hydroperoxide reductase from *Salmonella typhimurium*. 1. Purification and enzymatic activities of overexpressed AhpF and AhpC proteins, Biochemistry 35 (1996) 56–64.
[7] L.A. Tartaglia, G. Storz, M.H. Brodsky, A. Lai, B.N. Ames, Alkyl hydroperoxide reductase from *Salmonella typhimurium*. Sequence and homology to thioredoxin reductase and other flavoprotein disulfide oxidoreductases, J. Biol. Chem. 265 (1990) 10535–10540.
[8] Z.A. Wood, L.B. Poole, P.A. Karplus, Structure of intact AhpF reveals a mirrored thioredoxin-like active site and implies large domain rotations during catalysis, Biochemistry 40 (2001) 3900–3911.
[9] P.V. Dip, N. Kamariah, M.S.S. Manimekalai, W. Nartey, A.M. Balakrishna, F. Eisenhaber, B. Eisenhaber, G. Grüber, The ups and downs in AhpF: structure, mechanism and ensemble formation of the alkylhydroperoxide reductase subunits AhpC and AhpF from *Escherichia coli*, Acta Crystallogr. D Biol. Crystallogr. (2014) (manuscript No be5266, in press).
[10] Z.A. Wood, L.B. Poole, R.R. Hantgan, P.A. Karplus, Dimers to doughnuts: redox-sensitive oligomerization of 2-cysteine peroxiredoxins, Biochemistry 41 (2002) 5493–5504.
[11] Z.A. Wood, L.B. Poole, P.A. Karplus, Peroxiredoxin evolution and the regulation of hydrogen peroxide signaling, Science 300 (2003) 650–653.
[12] X. Wang, L. Wang, X. Wang, F. Sun, C.C. Wang, Structural insights into the peroxidase activity and inactivation of human peroxiredoxin 4, Biochem. J. 441 (2012) 113–118.
[13] M.S. Alphey, C.S. Bond, E. Tetaud, A.H. Fairlamb, W.N. Hunter, The structure of reduced tryparedoxin peroxidase reveals a decamer and insight into reactivity of 2Cys-peroxiredoxins, J. Mol. Biol. 300 (2000) 903–916.
[14] E. Schröder, J.A. Littlechild, A.A. Lebedev, N. Errington, A.A. Vagin, M.N. Isupov, Crystal structure of decameric 2-Cys peroxiredoxin from human erythrocytes at 1.7 Å resolution, Structure 8 (2000) 605–615.
[15] L.B. Poole, Bacterial defenses against oxidants: mechanistic features of cysteine-based peroxidases and their flavoprotein reductases, Arch. Biochem. Biophys. 433 (2005) 240–254.
[16] M. Aran, D. Caporaletti, A.M. Senn, M.T. Tellez de Iñon, M.R. Girotti, A.S. Llera, R.A. Wolosiuk, ATP-dependent modulation and autophosphorylation of rapeseed 2-Cys peroxiredoxin, FEBS J. 275 (2008) 1450–1463.
[17] J. König, M. Baier, F. Horling, U. Kahmann, G. Harris, P. Schürmann, K.-J. Dietz, The plant-specific function of 2-Cys peroxiredoxin-mediated detoxification of peroxides in the redox-hierarchy of photosynthetic electron flux, Proc. Natl. Acad. Sci. 99 (2002) 5738–5743.
[18] K. Kitano, Y. Niimura, Y. Nishiyama, K. Miki, Stimulation of peroxidase activity by decamerization related to ionic strength: AhpC protein from *Amphibacillus xylanus*, J. Biochem. 126 (1999) 313–319.
[19] G. Grüber, J. Godovac-Zimmermann, T.A. Link, Ü. Coskun, V.F. Rizzo, C. Betz, S.M. Bailer, Expression, purification, and characterization of subunit E, an essential subunit of the vacuolar ATPase, Biochem. Biophys. Res. Commun. 298 (2002) 383–391.
[20] U.K. Laemmli, Cleavage of structural proteins during the assembly of the head of bacteriophage T4, Nature 227 (1970) 680–685.
[21] G. Tang, L. Peng, P.R. Baldwin, D.S. Mann, W. Jiang, I. Rees, S.J. Ludtke, EMAN2: an extensible image processing suite for electron microscopy, J. Struct. Biol. 157 (2007) 38–46.
[22] X. Liu, W. Jiang, J. Jakana, W. Chiu, Averaging tens to hundreds of icosahedral particle images to resolve protein secondary structure elements using a multi-path simulated annealing optimization algorithm, J. Struct. Biol. 160 (2007) 11–27.
[23] E.F. Pettersen, T.D. Goddard, C.C. Huang, G.S. Couch, D.M. Greenblatt, E.C. Meng, T.E. Ferrin, UCSF chimera—a visualization system for exploratory research and analysis, J. Comput. Chem. 25 (2004) 1605–1612.
[24] J. Jancarik, S.-H. Kim, Sparse matrix sampling: a screening method for crystallization of proteins, J. Appl. Crystallogr. 24 (1991) 409–411.
[25] T.G. Battye, L. Kontogiannis, O. Johnson, H.R. Powell, A.G. Leslie, iMOSFLM: a new graphical interface for diffraction-image processing with MOSFLM, Acta Crystallogr. D Biol. Crystallogr. 67 (2011) 271–281.
[26] A.J. McCoy, R.W. Grosse-Kunstleve, P.D. Adams, M.D. Winn, L.C. Storoni, R.J. Read, Phaser crystallographic software, J. Appl. Crystallogr. 40 (2007) 658–674.
[27] R.A. Laskowski, M.W. MacArthur, D.S. Moss, J.M. Thornton, PROCHECK: a program to check the stereochemical quality of protein structures, J. Appl. Crystallogr. 26 (1993) 283–291.
[28] W. DeLano, The PyMOL Molecular Graphics System, DeLano Scientific, 2002.
[29] E. Krissinel, K. Henrick, Secondary-structure matching (SSM), a new tool for fast protein structure alignment in three dimensions, Acta Crystallogr. D Biol. Crystallogr. 60 (2004) 2256–2268.
[30] C. Hunke, W.J. Chen, H.J. Schafer, G. Grüber, Cloning, purification, and nucleotide-binding traits of the catalytic subunit A of the V_1V_O ATPase from *Aedes albopictus*, Protein Expr. Purif. 53 (2007) 378–383.
[31] S. Barranco-Medina, S. Kakorin, J.J. Lazaro, K.J. Dietz, Thermodynamics of the dimer–decamer transition of reduced human and plant 2-cys peroxiredoxin, Biochemistry 47 (2008) 7196–7204.
[32] J. König, H. Galliardt, P. Jutte, S. Schaper, L. Dittmann, K.J. Dietz, The conformational bases for the two functionalities of 2-cysteine peroxiredoxins as peroxidase and chaperone, J. Exp. Bot. 64 (2013) 3483–3497.
[33] P.J. Hillas, F.S. del Alba, J. Oyarzabal, A. Wilks, P.R. Ortiz De Montellano, The AhpC and AhpD antioxidant defense system of *Mycobacterium tuberculosis*, J. Biol. Chem. 275 (2000) 18801–18809.